DOI: https://doi.org/10.24425/amm.2024.150929

KUNDURTI SAI CHAND[1], AMBUJ SHARMA[1*]

FRICTION-ASSISTED ADDITIVE MANUFACTURING (FAAM) FOR MULTISTACK ALUMINUM AA6061-T6/ AA7075-T6 ARMOR PLATES: NUMERICAL INVESTIGATION, FABRICATION, AND CHARACTERIZATION

Composite armoring materials are generally fabricated using multiple layers of metallic and non-metallic materials such as titanium, steel, aluminum, ceramics, epoxy, resins, etc. Building these armor materials in the first place aims to withstand high-velocity bullets. Aluminum alloys are the best choice to offer increased mobility and excellent properties like a high strength-to-weight ratio, fracture toughness, and corrosion resistance. In this research, Forrestal and Warren scaling law techniques were employed to determine the optimal aluminum armor plate thickness to withstand 500 m/s velocity 7.62 mm projectile releasing from the pistol . FEA package Ansys was utilized for numerical simulations of bullet penetration, validating the results obtained from the scaling laws. After that, friction-assisted additive manufacturing (FAAM) was explored to build an AA6061/AA7075 laminated aluminum metal matrix composite (AMMC) for armor. Considering the plate thickness, the FAAM tool was designed with an optimum shoulder length, shoulder diameter, pin length, and pin diameter. Then the optimized process parameters were utilized to build the multi-stack armor plate using dissimilar aluminum alloys. Microstructural, and mechanical characterizations were conducted to assess the feasibility of the FAAM-built multi-stack armor plate. The findings of the work revealed better-refined grain's microstructural profile in comparison with base materials and resulted in higher tensile and micro-hardness results. FAAM build improved the mechanical strength and yield strength of the base alloy AA6061 by roughly 25% and 31%, respectively.

Keywords: Friction-assisted additive manufacturing; Aluminium alloys; Microstructural characterization; Multistack armor plate; Impact analysis

1. Introduction

Armor systems safeguard people and equipment from various hazards, such as gunshots, shrapnel, and explosives. Material selection for armor applications is critical since it impacts the overall performance of the armor system [1]. Due to its tremendous strength and durability, steel/titanium is one of the most utilized materials in armor applications such as naval and military vehicles. Also, because of their excellent hardness and heat resistance, ceramics such as alumina and silicon carbide are employed as vehicle add-on armor and stand-alone body armor systems [2]. Aramid fibers like Kevlar have high energy absorption characteristics, allowing them to scatter and absorb a bullet's kinetic energy, slowing it down and preventing penetration [3]. Unique composites have been developed recently to address the need for lightweight ballistic applications. However, single-material armored plates have their disadvantages. Therefore, researchers are striving hard to build multilayered armor plates. Multilayered configurations offer several advantages over single-material armor plates [4]. By combining different materials, the weaknesses of one material can be compensated for by the strengths of another – this improved resistance against different types of projectiles, including armor-piercing rounds. Various variables, such as the degree of the specific danger, weight restrictions, and the intended use of the armor plate, determine layering [5]. Researchers carefully evaluate these elements to achieve the combination of ideal protection, weight, and flexibility. One common approach in multilayered configurations is to have a front layer that is hard and rigid, such as ceramic or metal, which can break up or deform the bullet upon impact [6]. This initial layer helps distribute the impact force over a larger area, reducing the chance of penetration. Behind the front layer are usually additional layers made of materials with high tensile strength, such as aramid fibers (e.g., Kevlar) or ultra-high molecular weight polyethylene (UHMWPE). To ensure excellent protection from ballistic impacts, the armor systems are built with multiple layers, including a ceramic layer, steel layer, aluminum layer, and Kevlar layer, which raises the

[1] VIT-AP UNIVERSITY, SCHOOL OF MECHANICAL ENGINEERING, AMARAVATI, ANDHRA PRADESH, INDIA-522237

* Corresponding author: ambujsharma08@gmail.com)

total cost of armor [7]. To overcome the costs, the ceramic and steel layers can be replaced with lightweight aluminum alloys, reducing the areal density and the costs and offering similar ballistic protection [8].

Numerous researchers have investigated various numerical models to validate the aluminum alloy's capability to obstruct ballistic projectiles [9]. Out of all the research models, the scaling law technique designed by Forrestal et al. has shown almost closer results to the experimental results for aluminum alloys [10]. The ballistic limit velocity and the thickness of the plate were evaluated using this technique. After that, the desired combination of multilayered dissimilar aluminum alloy configuration is built so that the overall cost of the armor plate configured is also minimal compared to the ceramic and steel layers. The selection of the manufacturing technique to build an armor system per the design parameters obtained from the scaling law technique will play an essential role in achieving sound-quality armor.

Generally, traditional production methods have been used to build armor systems. Recently, a few of the research groups explored friction stir processing (FSP) to modify the surface properties of AMMC for armor applications [11]. Recently, additive manufacturing (AM) has been established as the best technology for building multiple stacks with minimal cost and less wastage [12]. Melt-based AM techniques such as VAT photopolymerization, material jetting, binder jetting, material extrusion, and powder bed fusion are used to build layer-by-layer stacks. However, these techniques have limitations requiring more energy, high production & maintenance cost, nonuniform microstructures, porous defects, and surface cracks [13]. Solid-state AM techniques such as ultrasonic AM, Additive friction stir deposition, and cold spry AM provide better builds, uniform microstructure, and fewer manufacturing defects [14]. Therefore, in recent years, solid-state AM has gained more attention in producing laminated AMMC [15-16]. From various solid-state AM techniques, the FAAM technique is the sophisticated method that combines the principles of Friction Stir Welding (FSW) and Friction Stir Processing (FSP) to create multiple layers with controlled microstructure [17-18]. This method combines stacks of multiple sheets using a non-consumable rotating tool. Initial research has yielded encouraging results regarding grain refinement, mechanical characteristics improvement, and defect reduction [19-20]. More scientific research is needed to fully comprehend the potential of FAAM to manufacture AMMCs for advanced engineering applications.

The use of FAAM for armor systems remains relatively unexplored. This study investigates the FAAM approach to develop a multi-stack aluminum armor plate to replace conventional steel/ceramic layers. Initially, numerical investigations are conducted to assess the potential of multilayered armor plates using different aluminum alloys. The scaling law technique evaluates the ballistic protection limit of AA6061-T6 and AA7075-T6 aluminum alloys. Subsequently, the ANSYS v19.2 AUTODYNE software package is utilized to estimate the residual velocity of a bullet upon impact with the designed armor plate configuration. Once the optimal configuration is determined using AUTODYNE, we delve into the fabrication techniques for constructing multilayered dissimilar aluminum alloy plates. The FAAM technique successfully produces faultless multilayered dissimilar aluminum alloy stacks. Extensive investigations are then carried out to evaluate the efficiency of the FAAM build, employing microstructural characterization techniques such as optical microscopy (O.M), scanning electron microscopy (SEM), and energy dispersion spectroscopy (EDS). Furthermore, mechanical tests, including tensile, microhardness, and impact tests, are performed to assess the efficacy of the overall FAAM multi-stack armor. Based on the evaluation, the desired thickness of the multi-stack armor plate is calculated as 18 mm, and thus the manufacturing plan is created utilizing the FAAM technique.

2. Numerical Analysis of AA6061-T6/AA7075-T6 multi-stack composite armor

2.1. Scaling Law for Ballistic Limit Velocities

In the present work, the scaling law technique derived by Forrestal et al. [21] was utilized to determine the appropriate thickness of metallic armor plate that can successfully hinder the penetration of the hard steel core projectile [22]. The equations for scaling laws were derived from cylindrical cavity expansion to replicate the formation of a ductile hole in the armor plate caused by the bullet piercing. These closed-form perforation equations for ogive nose hard steel core bullets that perforate into aluminum armor plates was validated with the experimental study [23]. This numerical model applies to any projectile impacting aluminum targets, regardless of bullet type or velocity. Commonly available ogive nose AMP2 7.62 mm bullets with 500 m/s striking velocity was considered for the impact analysis on AA6061-T6 and AA7075-T6 armor plates.

The ballistic limit velocities of armor materials based on plate thickness are computed from the perforation equation as

$$V_{bl} = K(\sigma_r * h)^{1/2} \tag{a}$$

where, V_{bl} is the ballistic-limit velocity, K is the constant, K = 109 (m/s) (GPa.mm)$^{1/2}$, h is the armor plate thickness. σ_r is the quasi-static radial stress required for ductile-hole growth by projectile perforation is defined as [24]:

$$\sigma_r = \frac{(Y.S)}{\sqrt{3}}\left\{1+\left[\frac{E}{\sqrt{3}(Y.S)}\right]^n \int_0^b \frac{(-\ln x)^n}{1-x}dx\right\} \tag{b}$$

$$b = 1-\gamma^2 \tag{c}$$

$$\gamma^2 = \frac{2(1+\vartheta)(Y.S)}{\sqrt{3}(E)} \tag{d}$$

where *Y.S.* is the yield strength, E is Young's modulus, n is the coefficient of determination for Lamber-Jonas curve fit, and ϑ is the poisons ratio of the respective armor material. The striking

TABLE 1

Material Properties of AA6061-T6 and AA7075-T6 used for Scaling Law Technique

Material type	Density (kg/m^3)	Youngs Modulus (E) GPa	Poisson's ratio (υ)	Yield Strength (Y.S) MPa	Coefficient of determination (n)	Reference
AA6061-T6	2700	68.9	0.33	276	0.084	[25]
AA7075-T6	2810	71.7	0.33	503	0.060	[26]
Steel Bullet	7850	200	0.29	470	—	[27]

velocity is considered equivalent to the ballistic limit velocity to determine the optimal thickness of the plate because armor absorbs the bullet's kinetic energy.

The material input data used in this analysis is represented in TABLE 1, and the output data like b, Quasi-static radial stress (σ_r) and the optimal plate thickness (**h**) determined by scaling law equations are represented in TABLE 2.

TABLE 2

Output data for AA6061-T6 and AA7075-T6

Material type	*b*	Quasi-static radial stress (σ_r) (GPa)	The thickness of the plate (*h*) (mm)
AA6061-T6	0.993848	1.17	17.98
AA7075-T6	0.98923	1.81	11.63

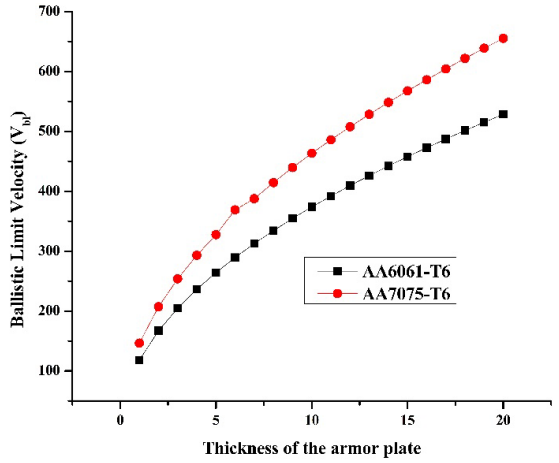

Fig. 1. Graph representing the ballistic limit Velocities vs. the thickness of the armor plate

Using the scaling law equations, the V_{bl} was estimated for AA6061-T6 and AA7075-T6 alloys for various plate thicknesses ranging from 1 mm to 20 mm, respectively, as shown in Fig. 1. From the graph in Fig. 1, it is evident that the optimal thickness of armor plates made of AA6061-T6 and AA7075-T6 are 17.98 mm and 11.63 mm thick, which can successfully obstruct the bullet impact velocity of 500 m/s. Also, based on these findings, it was decided to construct a multi-stack aluminum armor plate with a thickness of 18 mm by laying these two alloys in an alternative manner for the present investigation. After that, the drop in impact velocity of the bullet after the impact with the target plate is calculated using the FE package (Ansys – Explicit dynamics) for further examination.

2.2. FE simulation of armor plates

A three-dimensional FE model of AA6061, AA7075, and multitask armor plates were considered to perform numerical simulations of normal impacts of ogive nose hard steel core bullets (dimensions as shown in Fig. 2(a)) [29] on single and multilayered stacks of 18 mm thick aluminum armor. Dimensions of the aluminum armor are represented in Fig. 2(b, c). The multistack armor plate was arranged in a manner such as 6 mm thick AA6061-T6 was placed as the bottom plate, and further, the 3 mm thick alternative layers of AA7075-T6 and AA6061-T6 plates were stacked upon one another as shown in Fig. 2(c). The striking face of the armor plate will be the top layer, i.e., a 3 mm thick AA6061-T6 plateas shown in Fig. 2(c).

The material properties of AA6061-T6 and AA7075-T6 are mentioned in TABLE 1. Steel core bullet properties are

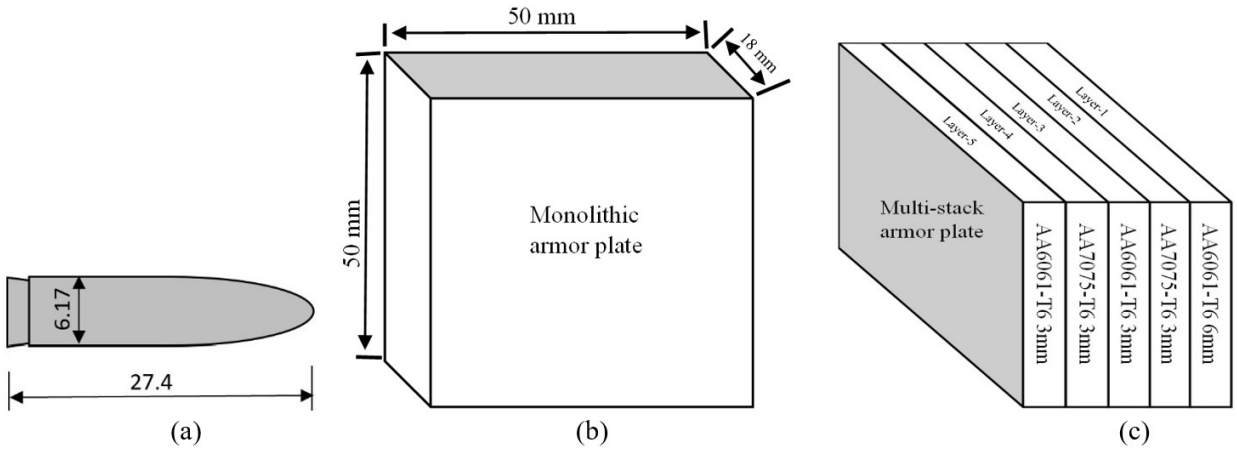

Fig. 2. (a) The geometry of the bullet (in mm), (b) Monolithic armor plate, (c) multilayered armor plate

ρ = 7850 kg/m^3; υ = 0.29; and E = 200 GPa. Typical snapshots of the bullet core and armor plate designed in space claim [30] are represented in Fig. 3. The distance measured between the bullet's tip and the armor plate was 150 mm. The body sizing method was used to mesh the bullet core and armor, as shown in Fig. 4. Ultra-fine meshes were used at the striking zone of the plate, whereas coarse mesh was used rest of the zone of the armor plate. The reason for considering the fine mesh at the centre is to reduce the simulation time. The bullet velocity of 500 m/s in the x-direction was considered for projectile perforation in the armor plate. The end time was 0.000336 μs for the distance between the bullet's tip and the armor plate's end. The parameters of the impact analysis, namely, the residual velocity of the bullet after perforation, were analysed in the post-processing step.

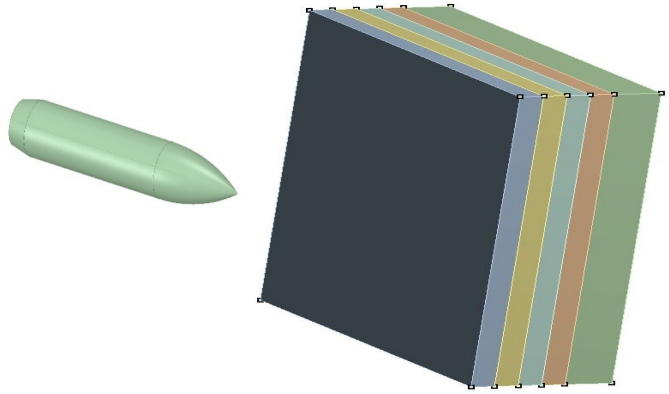

Fig. 3. Design of bullet and armor plate using Space Claim

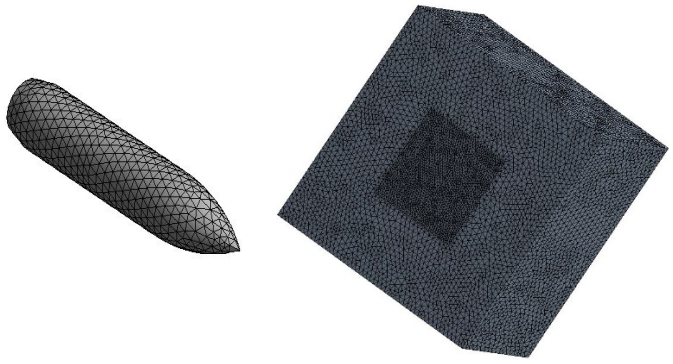

(a) (b)

Fig. 4. (a) Meshed model of bullet, (b) meshed model of armor plate

Fig. 5 compares a single-layer AA6061-T6, AA7075-T6, and multi-stack armor plates in terms of the residual velocity drop after a ballistic impact. The results reveal that the residual velocity decreases the most for the AA7075-T6 plate and the least for the AA6061-T6 plate, with the multi-stack layer showing a decrease in velocity closer to the AA7075-T6 plate. Since the multilayered stack armor plate provides similar ballistic protection as a single AA7075-T6 armor plate. The multi-stack plate can be best armor because it is a more cost-effective without sacrificing the appropriate level of protection, and it is also significantly less expensive than the AA7075-T6 plate.

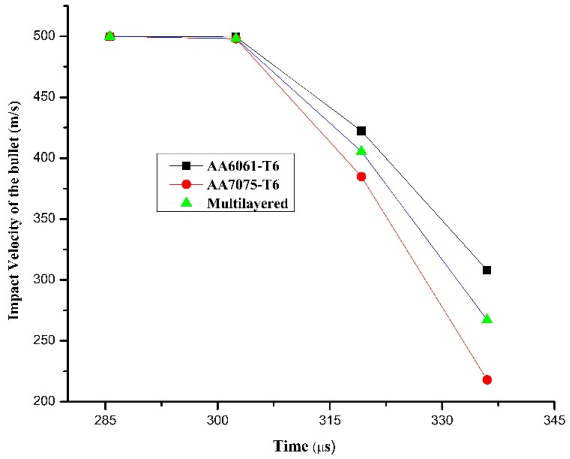

Fig. 5. Comparison of drop in bullet velocities after hitting the target plate of 18 mm thickness in all cases

3. Fabrication of 18 mm thick laminated AA6061/AA7075 AMMC using FAAM technique

FAAM technique was used to fabricate an 18 mm thick armor plate layer-wise using AA6061-T6 and AA7075-T6 sheets. The 18 mm multilayered configuration is constructed with a 6 mm thick bottom layer of AA6061, and the rest of the four layers, 3 mm thick, are stacked in an alternative manner, as represented in Fig. 6. The chemical compositions and mechanical characteristics of the AA6061-T6 & AA7075-T6 are represented in TABLES 3 and 4.

TABLE 3

Chemical composition of different grades of Al alloys used in the investigation

Materials	Cr	Cu	Fe	Mg	Mn	Si	Ti	Zn	Al
AA 6061-T6	0.12	0.25	0.59	1.93	0.10	0.74	0.08	0.09	Balance
AA 7075-T6	0.17	1.40	0.11	2.6	0.06	0.24	0.08	4.7	Balance

TABLE 4

Mechanical properties of different grades of Al alloys used in the investigation

Material	Yield Strength (MPa)	Tensile Strength (MPa)	Elongation (%)	Hardness (Hv)
AA6061-T6	274	310	17	106
AA7075-T6	502	572	11	172

FAAM is a repeating friction stir lap welding (FSLW) method that joins metal sheets one after the other by stacking them on top of previously lap-welded sheets. The FAAM method was carried out in this experiment using a hmt milling machine. Various clamping arrangements were used to closely hold the specimens to bear the greater loads, effectively managing the workpieces and minimizing process faults. To provide defect-free FAAM builds, the H13 tool with the flat threaded cylindrical pin profile was employed. This tool profile ensures

a smooth material flow during welding with no significant flaws. The H13 tool specifications were as follows: shoulder diameter 25 mm; shank diameter 18 mm; pin length 4.7 mm; pin diameter 6 mm. The optimized process parameters of tool rotational speed of 900 rpm, tool traverse speed of 40 mm/min, and a tool tilt angle of 2.5° were used to fabricate the 18 mm thick multistack armor plate. The tool pin plunge depth of 4.75 mm and the shoulder plunge depth of 0.15 mm was held constant throughout the procedure. Aluminum alloy sheets were initially positioned on the machine bed in a lap position and suitably secured without any gaps between the plates. After that, the revolving FAAM tool was moved forward for a length of 150 mm. The FAAM process was carried out in a single pass for every layer stacked on top of the other. These processes were repeated four times to create a 5-layer FAAM, as illustrated in Fig. 6. Advancing side (AS) is the side where the tool rotational direction is the same as the welding direction, and the Retreating side (RS) is the side where the tool rotational direction is opposite to the welding direction as shown in Fig. 6. In Fig. 6, where the bottom layer-1 is AA6061-T6 and layer-2 is AA7075-T6 was laid on top of the layer-1. In this manner, alternative layers of AA6061-T6 and AA7075-T6 were laid on top of each other until a 5-layered multistack armor plate was built, as shown in Fig. 6.

4. Specimen preparation for characterizations

Fig. 7(a). depicts the procedure for taking test samples from a full FAAM construction specimen for various microstructural, tensile, microhardness, impact, and scratch behavior characterizations. The samples were extracted from the FAAM-built via EDM machine. Each characterization was performed on two samples to evaluate the reproducibility of the results, and throughout the investigation, the average of the test results was considered for all the tests.

The metallographic samples were created in compliance with ASTM E3-95 [31] by extracting 35 mm×18 mm×10 mm samples from the FAAM build. The samples were next polished using emery sheets of various grades (150 to 3000 m) to remove scratches, followed by 0.25 µm diamond paste for mirror polishing. Keller's reagent [32] was used to etch the polished samples to study their macro and micro properties. The interfacial layers'

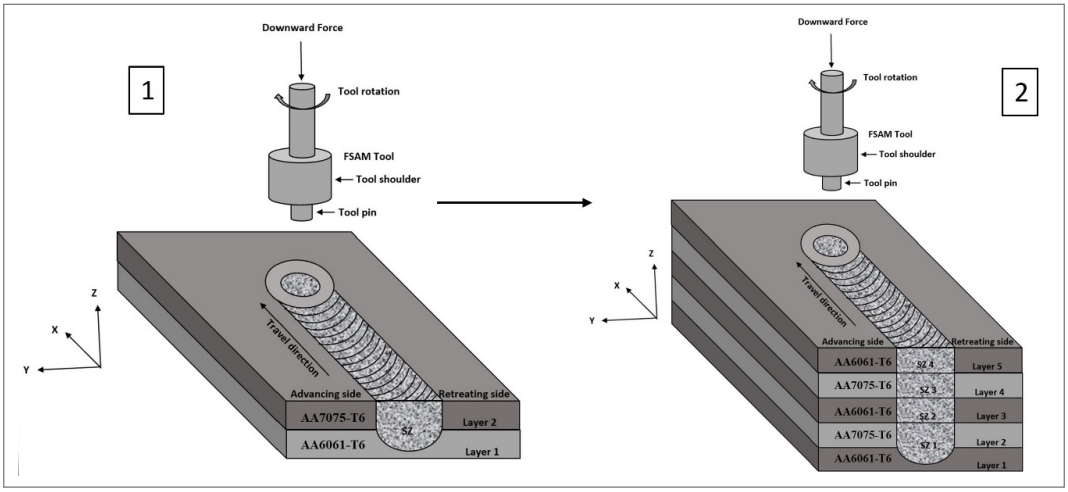

Fig. 6. Schematic Representation of FAAM Procedure along with the tool used for FAAM

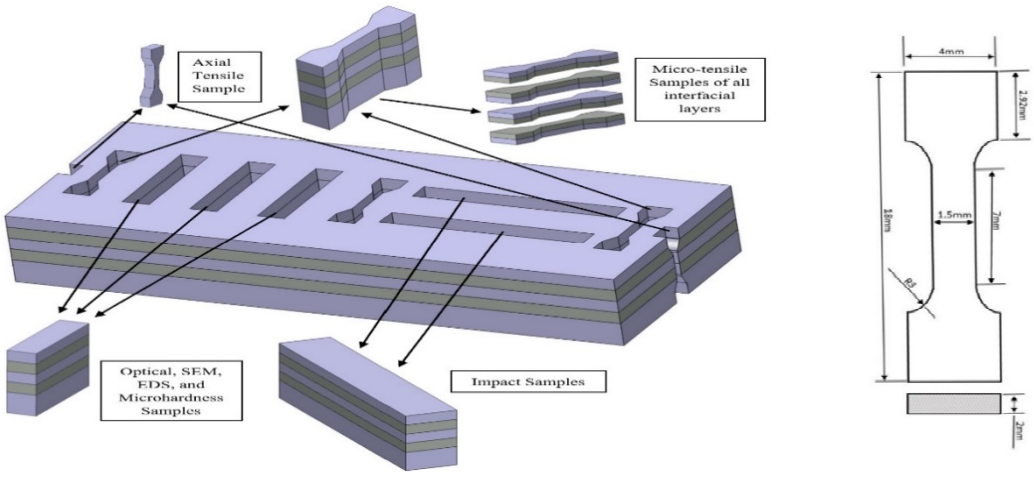

(a) (b)

Fig. 7. (a) Samples extraction procedure from FAAM build, (b) micro-tensile sample dimensions (mm)

microstructures and various FAAM construction zones were analyzed using the ZEISS Primotech metallurgical microscope. The FAAM specimens' microstructures and elemental composition were examined using a JCM-6000 plus scanning electron microscopy (SEM) with energy dispersive spectroscopy (EDS). The mechanical characteristics of the specimens were assessed to understand the structural performance of the FAAM armor plates. The samples' ultimate strength and yield strength were estimated using the universal testing equipment (H10KL). Standard micro tensile specimens were made into ASTM WK49229 standard [33], as shown in Fig. 7(b), and the test was carried out at room temperature with a strain rate of 1 mm/min. The Charpy test was used to measure the impact hardness of the FAAM construction. Furthermore, microhardness tests were performed on the Vickers Hardness Tester (METCO-VH-LMDX) using a square pyramid-type diamond indenter to examine hardness variation in all layers along the vertical (build) and horizontal directions.

5. Results and discussion

5.1. Morphological analysis

The FAAM microstructural analysis is a bit tricky since it comprises multiple layers of friction stir lap welds subjected to varied temperatures as they are stacked one on top of the other. After stacking up the initial layer, more stacks are joined over the top where the pin stirs. The temperature rises and spreads to the lower layers, revealing some fascinating outcomes in the microstructural study of the final FAAM structure. The final construction microstructure analysis depends entirely on the initial microstructure of the primary aluminum alloys. The microstructure of the base material demonstrates that the grains are coarser and banded along the direction of rolling, as illustrated in Fig. 8(a and b).

Morphological experiments are being conducted to determine the efficiency of FAAM in producing an armor plate made of different metals. To test the quality of the joints, optical macrographs and micrographs were analyzed. FSLW was used to stack layers, with the material on top sliding downward and elongating the hook throughout the dwell period. The tool stirs deeply into the bottom layer, allowing for effective stirring and the formation of joints between the layers in three zones: the Stir Zone (SZ), the Thermo-Mechanically Affected Zone (TMAZ), and the Heat Affected Zone (HAZ). The morphology of these zones was examined to assess the overall construction quality of the FAAM components, with a focus on the interfacial layers. Because they are exposed to several stirring motions and temperature variances along the build zone, the interfacial layers play a critical role in defining the overall build quality of the FAAM components. The macrograph is shown in Fig. 9(a). demonstrates that the optimized FAAM process parameters allow for the mixing of different materials, resulting in aproper metallurgical bonding between the layers without showing any defects throughout the FAAM build. The micrographs ofother regions like SZ, TMAZ, and HAZ of various interfacial layers shown in Fig. 9(b-d) show a homogeneous mixing of incompatible alloy constituents, with efficient dynamic recrystallization, coarsening, and grain refining occurring simultaneously. The micrographs also demonstrate that the SZ, TMAZ, and HAZ areas have finer grain sizes than the base alloy microstructures. The primary reason for grain refining was the variable temperature and mechanical stirring action during the FAAM process. The SEM micrograph shown in Fig. 9(e) at one of the interfacial layer regions demonstrates the material intermixing with an appropriate pattern, indicating perfect interfacial bonding between two alloy materials. The presence of Al and other alloying elements with a more significant proportion of Mg in the interfacial bonding between AA6061-T6 and AA7075-T6 was shown by EDS elemental mapping in Fig. 9(f).

5.2. Mechanical analysis

5.2.1. Tensile testing

A detailed tensile testing study was carried out to evaluate the strength of interfacial layers and the build direction of a sample produced by a cross-section of FAAM construction. The dimensions of the tensile specimen were carefully studied

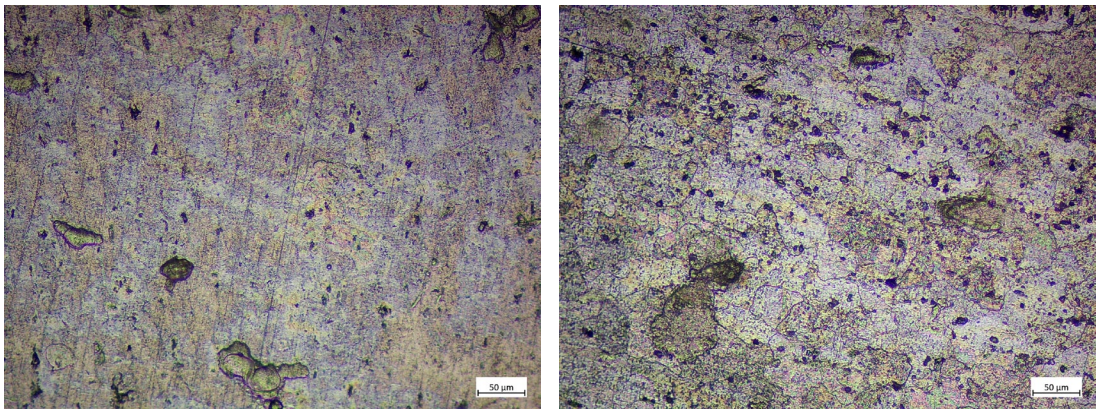

(a) (b)

Fig. 8. Optical Micrographs of base alloy materials: (a) AA6061-T6, (b) AA7075-T6

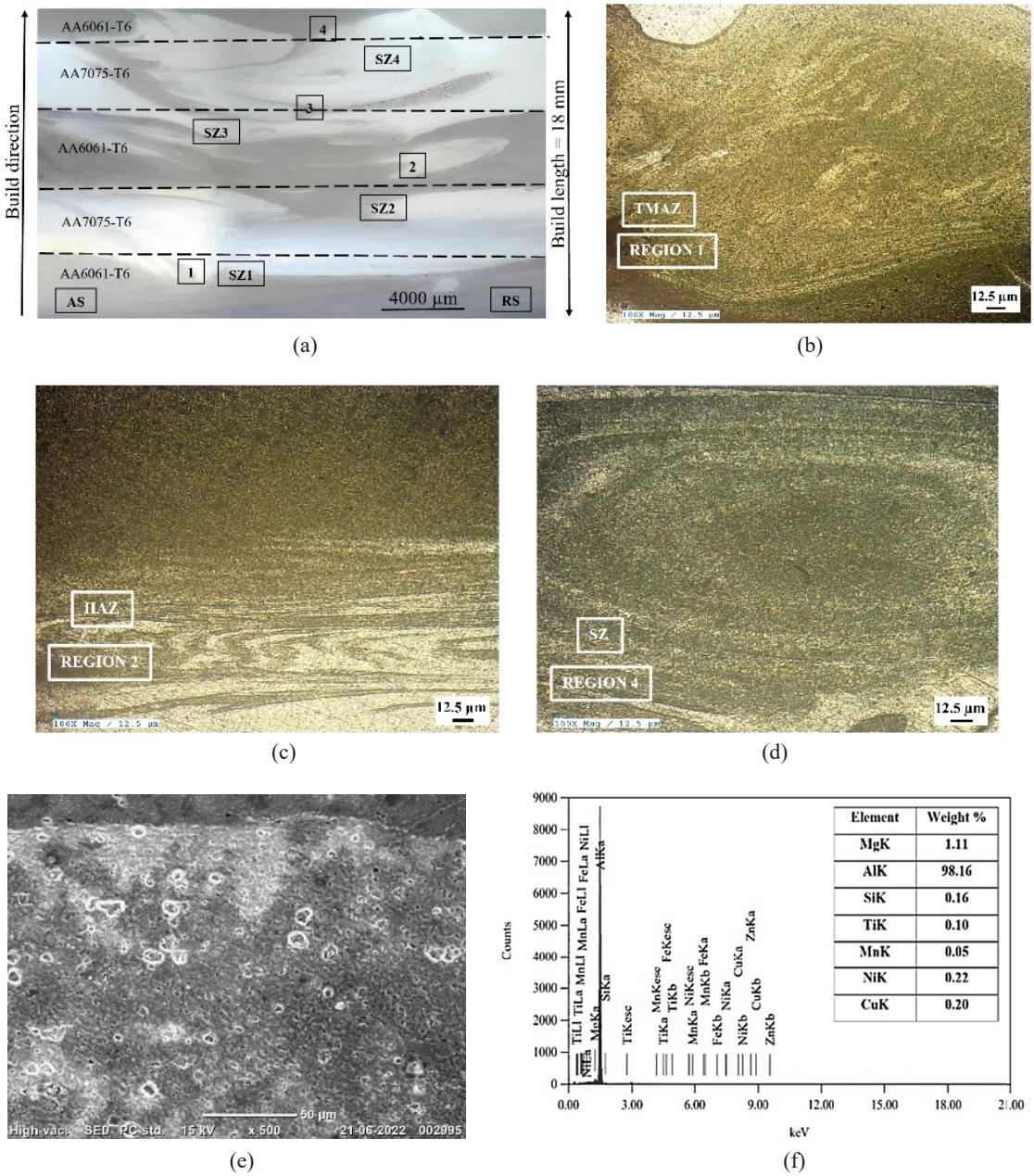

Fig. 9. (a) Macro-image of the cross-sectioned FAAM sample, (b) optical micrograph of region-1 showing the TMAZ of the FAAM cross-section, (c) optical micrograph of region-2 showing the HAZ of the FAAM cross-section, (d) optical micrograph of region-4 showing the SZ of the FAAM cross-section, (e) SEM micrograph of region-3 showing the SZ of the FAAM cross-section, (f) EDS elemental mapping results of region-4

to guarantee precise and dependable findings. The weldment strength was compared to the ultimate tensile strengths of the basic materials AA6061-T6 and AA7075-T6, which are 310 MPa and 572 MPa, respectively, in this investigation. The tensile test results revealed that the weldments demonstrated extraordinary strength compared to the tensile strength of the AA6061-T6

TABLE 5

Tensile properties of FAAM sample at different interfacial layers

Specimen	UTS (MPa)	Yield Strength (MPa)	Strain (%)	Fracture location center	Fracture mode
AA6061-T6 BM	310	274	17	Centre of gauge length	Ductile
AA7075-T6 BM	572	502	11	Centre of gauge length HAZ	Ductile
Interfacial layer – 1	304	272	10.5	Weld	Ductile
Interfacial layer – 2	332	308	9.56	HAZ Weld	Ductile
Interfacial layer – 3	375	350	8.8	HAZ Weld	Ductile
Interfacial layer – 4	394	364	8.22	HAZ Weld	Ductile
Axial Tensile Sample	386	360	8.6	Centre of gauge length	Ductile

base material and preserved 60-80% of the strength of the AA7075-T6 base material. It is worth noting that the interfacial layers' ultimate tensile strength (UTS) varied from one to the next, with strength rising from bottom to top. Interfacial layers (1-4) had UTSs of 304 MPa, 332 MPa, 374 MPa, and 394 MPa, respectively. The increased strength is attributed to the FAAM process's grain refining and annealing effects.

Similarly, the yield strength of the interfacial layers increased from bottom to top due to the same grain refining and annealing effects. These findings imply that FAAM can generate interfacial layers with high strength, and this technology might be applied in various applications. However, as shown in Fig. 10, the interfacial layer weldments' percentage elongation was 10-20% lower than the base alloys. This decrease in flexibility can be related to interfacial bonding behavior between two different alloy materials with high and low strengths, as well as the percentage elongation experienced during the FAAM process.

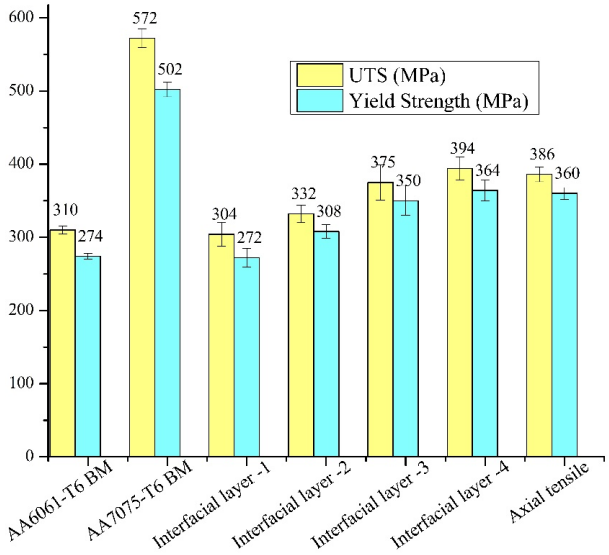

Fig. 10. Comparison of UTS (MPa), Yield Strength (MPa) of BM and FAAM build samples

The rotating tool's mechanical action induces severe plastic deformation in the material, resulting in dynamic recrystallization and smaller grain formation. This reduction in grain size enhances mechanical properties such as strength and ductility. The interfacial layers exhibit improved mechanical properties compared to the base alloys but may not precisely match either alloy. The gradual increase in strength from bottom to top suggests variations in microstructure or composition due to differential plastic deformation and heat input [34].

5.2.2. Microhardness testing

Microhardness measurements were performed to assess the FAAM construct's efficiency and comprehend the variance in microhardness across various layers. Horizontal microhardness tests were conducted from the bottom to the top layer from the AS to the RS (see dotted lines in the macro image shown in Fig. 11). The SZ exhibited much greater microhardness than the HAZ and TMAZ throughout all five construction layers, according to the data. Fig. 11. also revealed a more excellent hardness zone around the SZ on each layer of the FAAM construct, with a maximum hardness of 138.4 Hv recorded in the SZ of layer 4. This rise in hardness is due to the SZ undergoing extensive plastic deformation and constant dynamic recrystallizations, mainly at the layer interface, leading to a fine-grained microstructure. Because of its more robust resistance to deformation, the fine-grain size microstructural area has higher microhardness. While the FAAM builds retreating side (RS) had the lowest hardness, with 43.2 Hv found at the HAZ of layer1 measurement. This decrease in microhardness is due to grain development in the HAZ caused by the annealing action. Overall, the microhardness measurements revealed important information on the microstructure of the FAAM build and the difference in microhardness between layers. The variance in microhardness was primarily caused by microstructure variations found across the build direction due to a temperature gradient throughout the FAAM process [35].

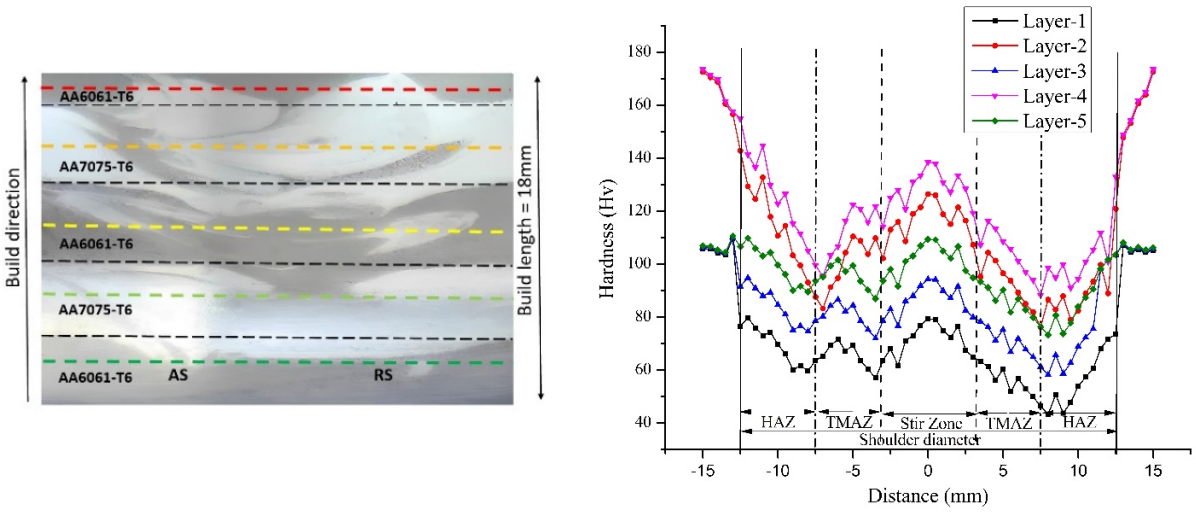

(a) (b)

Fig. 11. Microhardness in the horizontal direction for all layers in the build direction: (a) measuring locations, (b) measured data

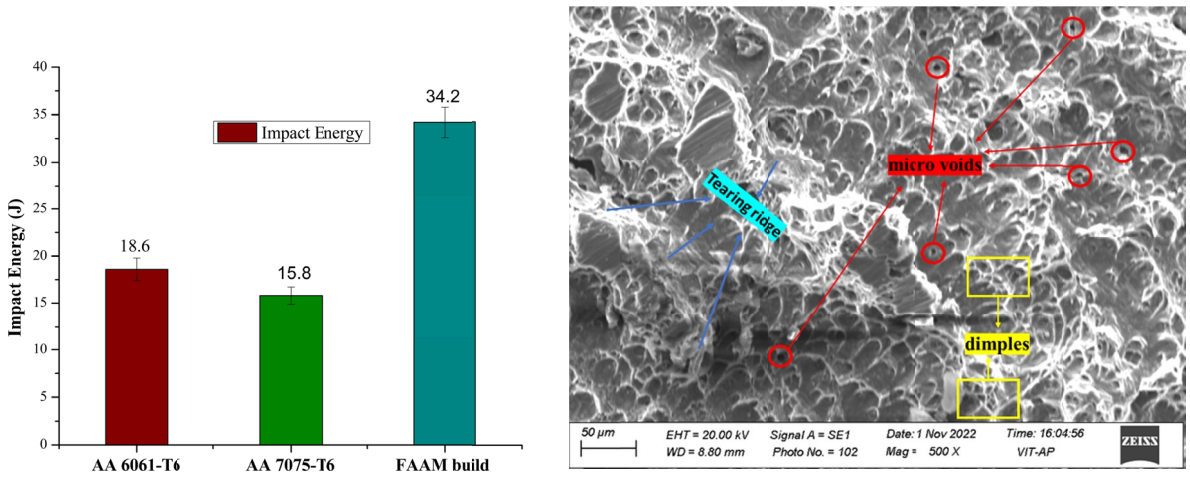

(a) (b)

Fig. 12. (a) Comparison of impact values of base materials and FAAM build material, (b) Fractography of FAAM build material

5.2.3. Impact testing

Charpy's test FAAM specimens designed for impact energy are evaluated at room temperature. The findings are shown in Fig. 12(a). From the results, the impact value for the FAAM build specimen has the highest impact energy at 34.2 J, while the base materials AA6061-T6 and AA7075-T6 have 18.6 J and 15.8 J, respectively. As a result, the toughness of the FAAM-built specimens is nearly double that of the base materials. High toughness can be attributed to heat treatment from linear friction welding and layering. Following the charpy impact test, the specimens are evaluated under SEM to understand their fracture behavior. The fractography shown in Fig. 12(b) depicts that the FAAM build has a ductile fracture and refined dimple sizes, indicating that the bonding between the interfacial layers is more vital than in the base materials, allowing the FAAM build to achieve a higher impact strength than the base materials.

6.Conclusions

In the present work, the ideal thickness of aluminum alloy armor plates and the residual velocity of bullets after impact are calculated using Forrestal and Warren scaling law approaches. FAAM build 5-layered 6061-T6/7075-T6 were fabricated successfully using optimum process parameters. The significant findings of the current investigation are given below:

i. The analysis of the numerical results indicates that the AA7075-T6 plate exhibits the highest reduction in residual velocity, followed by the multi-stack layer. In contrast, the AA6061-T6 plate demonstrates the least decrease in velocity. Notably, the multi-stack plate demonstrates a decrease in velocity that closely resembles that of the AA7075-T6 plate.
ii. Considering the ballistic protection offered by the multi-layered stack armor plate, which is comparable to that of a single AA7075-T6 armor plate, it is recommended to utilize the multi-stack plate instead of the AA7075-T6 plate.
iii. FAAM is an advanced solid-state AM method that can affordably produce completely gradient microstructure components.
iv. OM and SEM analysis revealed a fine-grained microstructure in the FAAM build. The FAAM process eliminates the difficulty of liquid-solid transition in fusion-based metal AM, resulting in a desired wrought microstructure.
v. Across the build cross-section, the 5-layered AA6061-T6/AA7075-T6 build component has stronger microhardness in the SZ and lower microhardness in the TMAZ and HAZ. A microhardness gradient has been observed across the build depth. The 6-7 interface SZ had the maximum microhardness of 138.4 Hv, while the bottom layer of the HAZ interface on the retreating side of the construction cross-section had the lowest hardness of 43.2 Hv.
vi. There was about an 80% improvement in impact strength between the FAAM-built sample and base alloys. The FAAM structure achieved an approximate impact energy of 34.2 J.

The enhancements in the FAAM build specimen results, especially better tensile strength, better microhardness, and better impact strength, result in the effective chances of fabricating multilayered armor using the FAAM technique.

7. Future Scope

FAAM is a novel method that combines the positive aspects of FSW with AM. A rotating tool mixes and extrudes material to form a 3D object. Although this technology is still in its early phases, there are many interesting possibilities for FAAM. FAAM offers the ability to generate products with superior material qualities compared to standard production processes. The procedure can decrease flaws, enhance strength, and improve material microstructure. As a result, FAAM might be utilized to create stronger, lighter, and more durable parts. This opens the door to developing novel materials and nanocomposites

that would be impossible to make using existing manufacturing processes. This brings up the possibility of creating customized components for specific purposes. Overall, FAAM has the potential to revolutionize the manufacturing business by enabling the production of complex parts with enhanced attributes in a more efficient, adaptable, and sustainable manner.

REFERENCES

[1] T. Nieberle, S.R. Kumar, A. Patnaik, C. Goswami, Adv. Eng. Des: Select Proceedings of ICOIED **2020**, 239-248 (2021). DOI: https://doi.org/10.1007/978-981-33-4018-3_22

[2] P.H. Silveira, T.T. Silva, M.P. Ribeiro, P.R. Rodrigues de Jesus, P.C. Credmann, A.V. Gomes, Acad. Lett **3742**, 1-11 (2021). DOI: https://doi.org/10.20935/AL3742

[3] G. Marsh, Reinf. Plast. **61** (2), 96-99 (2017). DOI: https://doi.org/10.1016/j.repl.2015.10.003

[4] M. Fejdyś, K. Kośla, A. Kucharska-Jastrząbek, M. Landwijt, Fibres Text. East. Eur. **3** (117), 79-89 (2016). DOI: https://doi.org/10.5604/12303666.1196616

[5] A. Pai, C.R. Kini, S. Shenoy, Thin-Walled Struct **179**, 109664 (2022). DOI: https://doi.org/10.1016/j.tws.2022.109664

[6] N.D. Andraskar, G. Tiwari, M.D. Goel, Ceram. Int., (2022). DOI: https://doi.org/10.1016/j.ceramint.2022.06.313

[7] R. Scazzosi, S.D. de Souza, S.C. Amico, M. Giglio, A. Manes, Compos. B. Eng. **230**, 109488 (2022). DOI: https://doi.org/10.1016/j.compositesb.2021.109488

[8] S. Siengchin, Def. Technol, (2023). DOI: https://doi.org/10.1016/j.dt.2023.02.025

[9] P. Si, Y. Liu, J. Yan, F. Bai, Z. Shi, F. Huang, Structures **48**, 1856-1867 (2023). DOI: https://doi.org/10.1016/j.istruc.2023.01.089

[10] T. Børvik, M.J. Forrestal, O.S. Hopperstad, T.L. Warren, M. Langseth, Int. J. Impact Eng, **36**(3), 426-437 (2009). DOI: https://doi.org/10.1016/j.ijimpeng.2008.02.004

[11] S.C. Kundurti, A. Sharma, P. Tambe, A. Kumar, Mater. Today **56**, 1468-1477 (2022). DOI: https://doi.org/10.1016/j.matpr.2021.12.337

[12] I. Gibson, D. Rosen, B. Stucker, M. Khorasani, D. Rosen, B. Stucker, M. Khorasani, Additive manufacturing technologies, 17, Springer Cham, Switzerland. DOI: https://doi.org/10.1007/978-3-030-56127-7

[13] K. Sanjeeviprakash, A.R. Kannan, N.S. Shanmugam, J. Braz. Soc. Mech. Sci. Eng. **45** (5), 241 (2023). DOI: https://doi.org/10.1007/s40430-023-04174-1

[14] R.S . Mishra, R.S. Haridas, P. Agrawal, Sci. Technol. Weld. Join. **27**(3), 141-165 (2022). DOI: https://doi.org/10.1080/13621718.2022.2027663

[15] A. Hassan, S.R. Pedapati, M. Awang, I.A. Soomro, Materials **16** (7), 2723 (2023). DOI: https://doi.org/10.3390/ma16072723

[16] A. Srivastava, N. Kumar, A.R. Kumar, Dixit, Mater. Sci. Eng. B **263**, 114832 (2021). DOI: https://doi.org/10.1016/j.mseb.2020.114832

[17] S. Choudhury, U. Acharya, J. Roy, B.S. Roy, Proc. Inst. Mech. Eng. E: J. Process Mech. Eng. **237** (2), 467-491 (2023). DOI: https://doi.org/10.1177/09544089221107755

[18] M. Srivastava, S. Rathee, Mater. Today: Proc. **39**, 1775-1780 (2021). DOI: https://doi.org/10.1016/j.matpr.2020.07.137

[19] S. Yan, L. Chen, A. Yob, D. Renshaw, K. Yang, M. Givord, D. Liang, J. Mater. Eng. Perform. **31** (8), 6183-6195 (2022). DOI: https://doi.org/10.1007/s11665-022-07114-7

[20] M. Srivastava, S. Rathee, S. Maheshwari, A.N. Siddiquee, T.K. Kundra, Crit. Rev. Solid State Mater. Sci. **44** (5), 345-377 (2019). DOI: https://doi.org/10.1080/10408436.2018.1490250

[21] M.J. Forrestal, T.L. Warren, Int. J. Impact Eng. **36** (2), 220-225 (2009). DOI: https://doi.org/10.1016/j.ijimpeng.2008.04.005

[22] T. Børvik, M.J. Forrestal, T.L. Warren, Exp. Mech. **50**, 969-978 (2010). DOI: https://doi.org/10.1007/s11340-009-9262-5

[23] M.J. Forrestal, T. Børvik, T.L. Warren, W. Chen, Exp. Mech. **54**, 471-481 (2014). DOI: https://doi.org/10.1007/s11340-013-9817-3

[24] M.J. Forrestal, B. Lim, W. Chen, Exp. Mech. **59**, 121-123 (2019). DOI: https://doi.org/10.1007/s11340-018-00442-7

[25] M.J. Forrestal, L.A. Romero, Int. J. Impact. Eng. **18**, 877-887 (2007). DOI: https://doi.org/10.1016/j.ijimpeng.2006.12.003

[26] M.J. Forrestal, T. Børvik, T.L. Warren, Exp. Mech. **50**, 1245-1251 (2010). DOI: https://doi.org/10.1007/s11340-009-9328-4

[27] T. Børvik, O.S. Hopperstad, T. Berstad, M. Langseth, Eur. J. Mech. A/Solids **20** (5), 685-712, (2001). DOI: https://doi.org/10.1016/S0997-7538(01)01157-3

[28] P. Rangacharyulu, B.V. Varma, S.S. Saran, I. Sudhakar, Mater. Today **5** (9), 19628-19637 (2018). DOI: https://doi.org/10.1016/j.matpr.2018.06.325

[29] M. Burkins, In 23rd International Symposium on Ballistics, (2007). DOI: http://www.ciar.org/ttk/mbt/papers/isb2007/paper.x.isb2007.TB11.ballistic_performance_of_thin_titanium_plates.burkins.2007.pdf

[30] X. Chen, Y. Liu, Finite element modeling and simulation with ANSYS Workbench, CRC press, (2018). DOI: https://doi.org/10.1201/9781351045872

[31] ASTM E3-95-Standard Practice for Preparation of Metallographic Specimens, ASTM International, (2001).

[32] M. Mohammadtaheri, Metallogr. Microstruct. Anal. **1**, 224-226. (2012). DOI: https://doi.org/10.1007/s13632-012-0033-9

[33] WK49229, A.S.T.M, New Guide for Orientation and Location Dependence Mechanical Properties for Metal Additive Manufacturing. Work in Progress, (2015).

[34] K.K. Jha, R. Kesharwani, M. Imam, Trans. Indian Inst. Met. **76** (2), 323-333 (2023). DOI: https://doi.org/10.1007/s12666-022-02672-9

[35] K.K. Jha, R. Kesharwani, M. Imam, Mater. Today: Proc. **5**6, 819-825 (2022). DOI: https://doi.org/10.1016/j.matpr.2022.02.262